Characterisation of Ring Testing in the Design of Offshore Oil Transportation Systems

Federico Guarracino[1,*] and Aldo Giordano[2]

[1]*Department of Structural Engineering, University of Naples "Federico II", Napoli - Italy*

[2]*Ideas srl, Napoli - Italy*

Abstract: The manufacturing procedure qualification tests (MPQT) of offshore pipelines projects has recently started to rely on ring collapse tests, which consist in testing a short section (50 mm) of a full scale joint. This approach is capable of providing valuable insight into the collapse behaviour of offshore pipelines and has practical, financial and logistic benefits.

Detailed analytical and numerical work has been carried out in order to understand the collapse mechanisms and the influence of several parameters, like geometry, material strength and seal friction, on the collapse behaviour has been investigated.

It is found that the shape of the initial imperfection and the seal friction can both affect the collapse and produce a variation in the value of the collapsing pressure.

Keywords: Ring collapse test, pipe qualification, out of roundness, seal friction, plastic buckling.

1. INTRODUCTION

In deep and ultra-deep waters the diameter of trunk lines coupled with the hydrostatic pressure tends to lead to failure of the pipeline by external collapse. This failure mode is an instability phenomenon that is governed by the geometry of the pipeline and its material properties. Failure of a pipeline section is dependent on many factors and as such the collapse pressure is very difficult to determine. Finite element techniques can allow the estimation of collapse where the actual geometry and material properties are known but in reality shape and properties vary along the pipe length, around the circumference as well as through the wall thickness.

To enable effective design work to be performed, and proven during service, it is necessary to ensure that the mechanical and dimensional properties of the pipe are controlled within very strict boundaries. More recently, and in collaboration with SAGE (Middle East to India Pipeline), a test method has been developed that allows the determination of pipe collapse pressures through the application of external pressure to rings of pipe materials [1]. This test method has been demonstrated to correlate well with full scale collapse data and it is proposed that this technique becomes a potential addition to pipe release testing procedures.

In fact full-scale tests performed using complete pipe joints are very expensive and only a limited number of test facilities can perform them. Moreover, the experimental setting must be accurately designed and controlled, since the boundary conditions can adversely affect the results under some circumstances [2-4].

In order to reduce the dependency on such full-scale tests, an experimental method has been developed for the collapse of ring samples that can be taken from production pipes. The test apparatus and the results from these tests are analysed in depth in this work.

2. EQUIPMENT AND TEST PROCEDURE

Figure **1** shows a section through the ring test equipment [1].

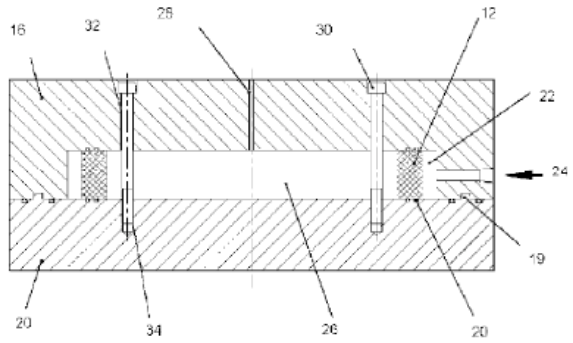

Figure 1: Section through the ring test equipment [1].

The test ring (12) is held between two effectively rigid plates, (16 and 20). The two halves of the pressure test chamber 16 and 20 are provided with

*Address correspondence to this author at the Department of Structural Engineering, University of Naples "Federico II", Napoli–Italy;
Tel: +390817683733; Fax: +390817683332; E-mail: fguarrac@unina.it

E-ISSN: 2409-787X/15

locating spigots (19) that correspond to locating holes with associated seals (21) to allow location of the two halves. O-ring seals (20) are located in the top and bottom sections. The central void (26) inside the test ring (12) is vented to atmosphere through a bleed hole (28) which is of sufficiently large diameter to also provide access for any strain gauge instrumentation (not shown) on the inner cylindrical surface of the test ring (12). The plates (16 and 20) are bolted together and the pressure is introduced into the space marked (22). In fact, the plates (16 and 20) are engaged by the test ring (12) to form an annulus accessible by a supply of pressurised hydraulic test fluid through an appropriate inlet port (24). The screws (30) extend through holes (32) in the top section (16) and pass through the void (26) to engage in threaded bores (34) in the bottom section (20). The pressure is retained in the space by the O-rings between the surface of the plate and the edge of the ring. The O-rings allow the ring to move relative to the plates while still maintaining a pressure seal.

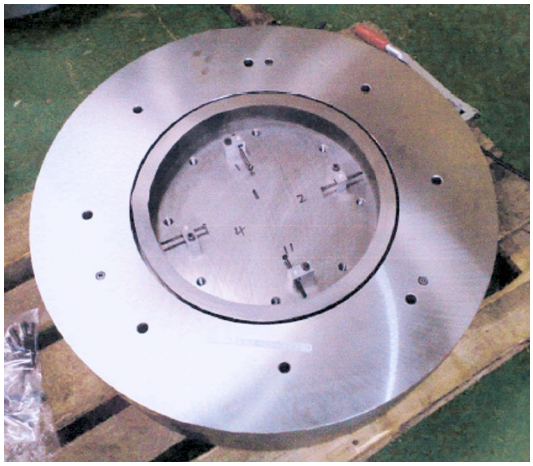

Figure 2: Lower plate with the test ring positioned in the test cavity.

The inner surface of the ring is open to the atmosphere. The ring is fitted with four strain gauges equally-spaced around the inner surface of the ring. Four displacement transducers are also attached to the inner surface of the ring at positions between the strain gauges (see Figure **3**).

The test procedure is as follows: rings are positioned in the bottom plate of the equipment and then the top plate is placed over it and bolted in position. The instruments are connected and set to zero. The pressurising fluid is introduced into the space between the outer surface of the rings and the test plate and the pressure is gradually increased in a controlled manner. As the applied load reaches the collapse limit, the pressure suddenly reduces and with continued addition of fluid the ring collapses.

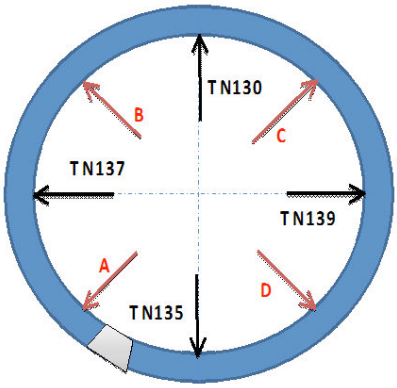

Figure 3: Placement of strain gauges (A-B) and displacement transducers (TN130-139).

3. RESULTS FROM EXPERIMENTS

The results from four different circular beams machined at Tata Steel [5] from the same pipe of diameter *D=457.2mm* and thickness *t=31.75mm,* are shown in Figure **4**, where the displacements are referred to four transducers placed at 0, π /2, π and 3π /2 positions, see Figure **3**.

The first three cases, namely (a), (b) and (c), show a limit pressure consistently ranging from 67.6 to 69.5 MPa, while the last one, (d), shows a limit pressure of 55.4 MPa.

This kind of behaviour has been repeatedly found and reported, to various degrees, also in additional instances, such as the Oman India test program [6] and the South Stream Offshore Pipeline FEED [7] and the need to understand the possible causes of such findings has led to the present investigation into the mechanics of the problem. The attention is focused on three different reckonable parameters, i.e. initial out-of-roundness of the ring, variation of the material properties of the pipe, friction between O-rings and the plates of the test rig.

4. GEOMETRICAL MEASUREMENTS OF THE OUT-OF-ROUNDNESS.

Out-of-roundness (OOR) in many design codes is defined in terms of a parameter involving the maximum, minimum and nominal diameters of a structure. For example, in DNV-OS-F101 Submarine Pipeline Systems [8] the ovality parameter is given by

$$\frac{D_{\max} - D_{\min}}{D_{nom}} \quad (1)$$

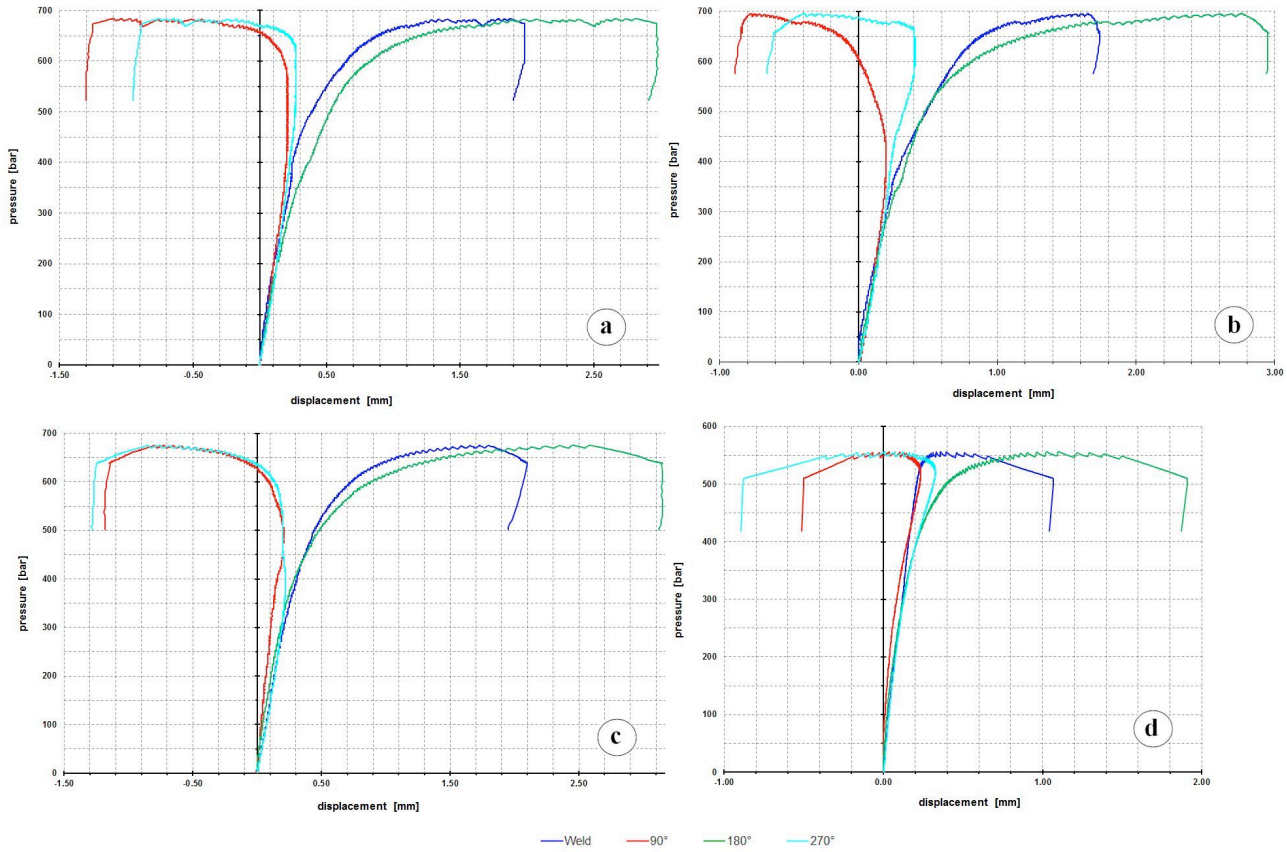

Figure 4: Measured radial displacements against the applied pressure for four different rings machined from the same pipe (*D=457.2mm, t=31.75mm*).

where $D_{\max}$, $D_{\min}$ and D_{nom} are, respectively the maximum, minimum and nominal diameters of the structure.

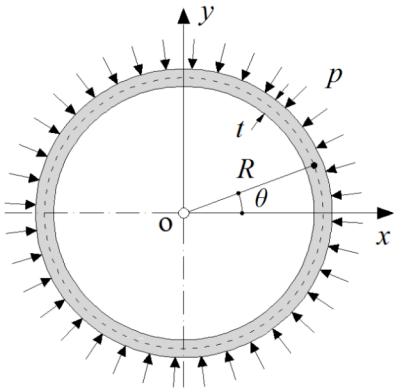

Figure 5: A ring under external pressure. The displacement field is expressed in terms of the radial component, $w = w(\theta)$.

However, the analyses conducted in some previous works by one of the present authors [9-11] suggest that it is important to be able to quantify not only the degree of out-of-roundness of pipes and rings if an accurate estimate of their strength is to be attained. In particular with reference to Figure **5**, it was found that in the case of UOE formed pipes a three-wave shape component of the type $\overline{w}_i \cos 3\theta$, where $\overline{w}_i$ is the imperfection amplitude, is very likely to play an important role, along with the traditional elliptical shape (see Figure **6**), in the collapse of the structural element under external pressure.

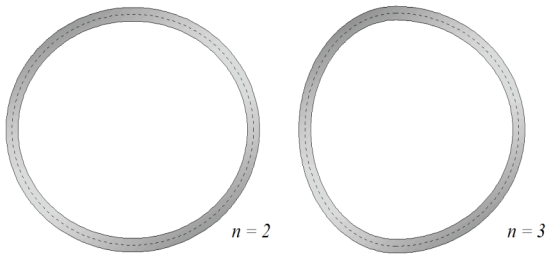

Figure 6: Sample OOR component shapes of the type $\overline{w}_i \cos n_i\theta$ for $n_i = 2$ (left) and $n_i = 3$ (right).

Out-of-roundness can be measured using a FARO® scanning arm [12]. The FARO® data are provided as a set of Cartesian coordinates (x_i, y_i), each corresponding to a measured point on the internal or on the external profile of the ring to be tested. Since radial displacements are of most interest to the problem, defining an out-of-roundness shape based on

deviations in radius from a fictitious reference circular shape is the most logical choice. To do this the centre of the nominal cross-section of ring is first located. The centre of the circle that best fits the mapped FARO® readings can be considered, to a good approximation, at the centre-of-mass of the set of measured points, located at (x_C, y_C).

In order to evaluate which imperfection shape of the type

$$\bar{w}(\theta) = \bar{w}_i \cos(n_i\theta + \psi_i) \qquad n_i \in \mathbb{N} \tag{2}$$

(where n_i is the number of waves and $\bar{w}_i$ and ψ_i are the amplitude and phase angles, respectively) can be considered more representative of the actual out-of-roundness of a ring a straightforward error function, Γ, has been proposed [11].

This method of analysis of geometric imperfection has been applied to eleven rings samples, taken from three UOE pipes from a typical deep water pipeline project at the Tata Steel facilities in Rotherham, UK. The nominal pipe size was *D=660mm,* with thickness *t=37.1mm*. The material was nominally X70 steel, but several material samples were subjected to compressive tests in order to define accurately the stress-strain curves. Some parameters which average the material properties for each pipe are listed in Table **1** along with the ring samples.

The eleven rings were tested and Table **1** collects the measured collapse pressures along with the ones calculated as in [9], both in the $n_i = 2$ and $n_i = 3$ imperfection case. Since the tested rings presented a nominal ovality, see Eq.(1), of 0.0001 ± 0.00002, in order to simplify the comparison the calculations were performed making reference to an averaged nominal ovality of 0.1%.

As it can be immediately noticed, in all the examined cases the calculated collapse pressures for an initial imperfection shape of the type $\bar{w}_i \cos 2\theta$ are below the measured ones, whereas those calculated for an initial imperfection shape of the type $\bar{w}_i \cos 3\theta$ are generally in good accordance with the actual ones.

It can be thus hypothesised that in the case of the tested UOE formed pipes the three-wave component of the shape imperfection plays an important role in contributing to the carrying capacity of the ring up to the limit value of the external pressure. In other words, in the beginning the structure would tend to withstand the applied pressure according to the eigensolution of the underlying elastic buckling problem corresponding the initial imperfection shape, before switching in the final stage of the collapse to the lowest eigenvalue, that is that characterised by a two-wave eigenmode.

In order to corroborate this assumption from a purely geometrical standpoint, all the scanned profiles

Table 1: Summary of Ring Data and Results from Collapse Tests [5]

Pipe ID	Ring ID	No of Scanned Points	0.2% PS(MPa)	0.5% RT (MPa)	Stress at 2%	Young Modulus (MPa)	Actual Collapse Pressure (MPa)	Calculated Collapse Pressure (MPa)
01	01B	818 (OD) 729 (ID)	406	445	583	238	59.68	61.72 (n_i = 3) 51.56 (n_i = 2)
01	01C	721 (OD) 684 (ID)	406	445	583	238	59.86	61.72 (n_i = 3) 51.56 (n_i = 2)
01	01D	807 (OD) 729 (ID)	406	445	583	238	59.41	61.72 (n_i = 3) 51.56 (n_i = 2)
01	01E	728 (OD) 700 (ID)	406	445	583	238	54.23	61.72 (n_i = 3) 51.56 (n_i = 2)
01	01F	862 (OD) 761 (ID)	406	445	583	238	61.88	61.72 (n_i = 3) 51.56 (n_i = 2)
02	02B	735 (OD) 729 (ID)	396	435	572	219	56.82	58.73 (n_i = 3) 48.97 (n_i = 2)
02	02C	877 (OD) 645 (ID)	396	435	572	219	57.06	58.73 (n_i = 3) 48.97 (n_i = 2)
02	02D	810 (OD) 657 (ID)	396	435	572	219	57.16	58.73 (n_i = 3) 48.97 (n_i = 2)
03	03B	885 (OD) 779 (ID)	382	419	543	202	50.99	51.37 (n_i = 3) 42.49 (n_i = 2)
03	03C	900 (OD) 697 (ID)	382	419	543	202	49.49	51.37 (n_i = 3) 42.49 (n_i = 2)
03	03D	767 (OD) 675 (ID)	382	419	543	202	50.78	51.37 (n_i = 3) 42.49 (n_i = 2)

Table 2: Summary of the Results from the Geometric Analysis of FARO® Scanned Profiles

Ring profile ID	01B(OD)	01C(OD)	01D(OD)	01E(OD)	01F(OD)	02B(OD)	02C(OD)	02D(OD)	03B(OD)	03C(OD)	03D(OD)
$\frac{\bar{w}_i}{R}$ $(n_i = 2)$	0.19 $\times 10^{-3}$	0.12 $\times 10^{-5}$	0.69 $\times 10^{-5}$	0.33 $\times 10^{-4}$	0.39 $\times 10^{-3}$	0.16 $\times 10^{-3}$	0.63 $\times 10^{-4}$	0.34 $\times 10^{-3}$	0.22 $\times 10^{-3}$	0.32 $\times 10^{-3}$	0.97 $\times 10^{-4}$
$\frac{\bar{w}_i}{R}$ $(n_i = 3)$	0.35 $\times 10^{-3}$	0.46 $\times 10^{-3}$	0.39 $\times 10^{-3}$	0.51 $\times 10^{-3}$	0.45 $\times 10^{-3}$	0.23 $\times 10^{-3}$	0.53 $\times 10^{-3}$	0.73 $\times 10^{-3}$	0.45 $\times 10^{-3}$	0.59 $\times 10^{-3}$	0.81 $\times 10^{-3}$
$\Gamma_3^{\min} / \Gamma_2^{\min}$	<1	<1	<1	<1	<1	≈1	<1	<1	<1	<1	<1
Ring profile ID	**01B (ID)**	**01C (ID)**	**01D (ID)**	**01E (ID)**	**01F (ID)**	**02B (ID)**	**02C (ID)**	**02D (ID)**	**03B (ID)**	**03C (ID)**	**03D (ID)**
$\frac{w_o}{R}$ $(n_i = 2)$	0.17 $\times 10^{-5}$	0.19 $\times 10^{-5}$	0.12 $\times 10^{-5}$	0.13 $\times 10^{-5}$	0.32 $\times 10^{-3}$	0.17 $\times 10^{-3}$	0.10 $\times 10^{-5}$	0.27 $\times 10^{-3}$	0.27 $\times 10^{-3}$	0.18 $\times 10^{-3}$	0.27 $\times 10^{-3}$
$\frac{w_o}{R}$ $(n_i = 3)$	0.20 $\times 10^{-3}$	0.34 $\times 10^{-3}$	0.21 $\times 10^{-3}$	0.28 $\times 10^{-3}$	0.27 $\times 10^{-3}$	0.19 $\times 10^{-3}$	0.47 $\times 10^{-3}$	0.39 $\times 10^{-3}$	0.39 $\times 10^{-3}$	0.34 $\times 10^{-3}$	0.61 $\times 10^{-3}$
$\Gamma_3^{\min} / \Gamma_2^{\min}$	<1	<1	<1	<1	>1	≈1	<1	<1	≈1	<1	<1

of Table **1** were analysed by means of the procedure illustrated in [11]. Table **2** collects all the results from the analysis of the scanned external (OD) and internal (ID) profiles of the eleven rings under consideration.

It is immediate to notice that seventeen of the analysed profiles show a better fit of a three-wave imperfection shape than of a two-wave one. This is given by the best fit error function ratio $\Gamma_3^{\min} / \Gamma_2^{\min}$. In three cases the fit can be considered equivalent for $n_i = 2$ and $n_i = 3$ and only in a case (internal profile of the sample 01F) a two-wave shape results a better fit than a three-wave one. Importantly, with the sole exception of the internal profile of the sample 01F, the imperfection amplitudes of the three-wave fitting shape are found to be higher than those of the two-wave fitting shapes.

5. ANALYSIS OF MIXED-MODE IMPERFECTIONS

The influence of mixed-mode imperfections modelled as in Eq.(2) has been analysed by means of a commercial Finite Element (FE) package [13].

In general, numerical investigation of the nonlinear behaviour of structures must follow the equilibrium path, identifying and computing the singular points like limit or bifurcation points, whose secondary branches in the equilibrium path must be examined and followed and this procedure can be adversely affected by any kind of approximation, as shown even in the simplest examples [14, 15]. To overcome difficulties with limit points, displacement control techniques were introduced and for this reason the modified arc-length method was used to follow the load-deformation path [16, 17].

The case studies taken into consideration are those of a ring characterised by a diameter of 457.2 mm and cross section 31.75 x 50 mm, see Section 3. The material properties are the following: $E = 206.6GPa$, $\sigma_y = 561MPa$, $\varepsilon_y = 0.01$, $\beta = 7.625$.

According to the measurements reported in the previous Section, it is assumed that the prominent imperfection modes are those characterised by two (n_i = 2) and three (n_i = 3) waves and, without lack of generality, the analysis has been performed on a combination of these imperfection modes only, i.e.

$$\bar{w}(\theta) = \sum_{i=1}^{2} \bar{w}_i \cos(n_i \theta + \psi_i), \qquad n_i \in \{2,3\} \tag{3}$$

The results are summarised in Table **3**. The influence of mixing initial imperfection modes varies with their relative amplitude and offset, but the increment in the buckling load deriving from the presence of the mode $n_2 = 3$ does not result always proportional to its weight and provides the value of 67.764 MPa, in line with the results from Figure **4** (**a-c**), only for $\bar{w}_1 = 0$, that is when the contribution from the lowest buckling mode is very low or nearly negligible.

Figures **7** and **8**, show both the load-displacement plot and the deformation at collapse from FE analyses for the limit cases of pure two and pure three waves initial imperfection.

Table 3: Collapse Pressure Depending on Mixed Shape Imperfection ($D = 457.2\,mm,\ t = 31.75\,mm,\ h = 50mm,\ w = 1/1000$) $W = 1/1000$)

$n_1 = 2$	$n_2 = 3$	*Pcrit [MPa]*
$\bar{w}_1 = \omega R\ ,\ \psi_1 = 0$	$\bar{w}_2 = 0\ ,\ \psi_2 = 0$	56.046
$\bar{w}_1 = 0.75\omega R\ ,\ \psi_1 = 0$	$\bar{w}_2 = 0.25\omega R\ ,\ \psi_2 = 0$	56.620
$\bar{w}_1 = 0.75\omega R\ ,\ \psi_1 = 0$	$\bar{w}_2 = 0.25\omega R\ ,\ \psi_2 = \pi/3$	56.621
$\bar{w}_1 = 0.75\omega R\ ,\ \psi_1 = 0$	$\bar{w}_2 = 0.25\omega R\ ,\ \psi_2 = \pi/2$	56.623
$\bar{w}_1 = 0.75\omega R\ ,\ \psi_1 = 0$	$\bar{w}_2 = 0.25\omega R\ ,\ \psi_2 = 2\pi/3$	56.626
$\bar{w}_1 = 0.5\omega R\ ,\ \psi_1 = 0$	$\bar{w}_2 = 0.5\omega R\ ,\ \psi_2 = 0$	57.085
$\bar{w}_1 = 0.5\omega R\ ,\ \psi_1 = 0$	$\bar{w}_2 = 0.5\omega R\ ,\ \psi_2 = \pi/3$	59.432
$\bar{w}_1 = 0.5\omega R\ ,\ \psi_1 = 0$	$\bar{w}_2 = 0.5\omega R\ ,\ \psi_2 = \pi/2$	57.116
$\bar{w}_1 = 0.5\omega R\ ,\ \psi_1 = 0$	$\bar{w}_2 = 0.5\omega R\ ,\ \psi_2 = 2\pi/3$	57.120
$\bar{w}_1 = 0.25\omega R\ ,\ \psi_1 = 0$	$\bar{w}_2 = 0.75\omega R\ ,\ \psi_2 = 0$	60.310
$\bar{w}_1 = 0.25\omega R\ ,\ \psi_1 = 0$	$\bar{w}_2 = 0.75\omega R\ ,\ \psi_2 = \pi/3$	57.712
$\bar{w}_1 = 0.25\omega R\ ,\ \psi_1 = 0$	$\bar{w}_2 = 0.75\omega R\ ,\ \psi_2 = \pi/2$	57.727
$\bar{w}_1 = 0.25\omega R\ ,\ \psi_1 = 0$	$\bar{w}_2 = 0.75\omega R\ ,\ \psi_2 = 2\pi/3$	57.744
$\bar{w}_1 = 0\ ,\ \psi_1 = 0$	$\bar{w}_2 = \omega R\ ,\ \psi_2 = 0$	67.764

From the analysis it can be inferred that the circular beams tested in cases (**a-c**) of Figure **4** are likely to have been shaped in the manufacturing process with a predominant three waves imperfection.

6. MATERIAL INHOMOGENEITY

In order to account for the variation of the material properties along the ring circumference, according to the analytical solutions provided in [11], for the sake of simplicity three different material regions, symmetric

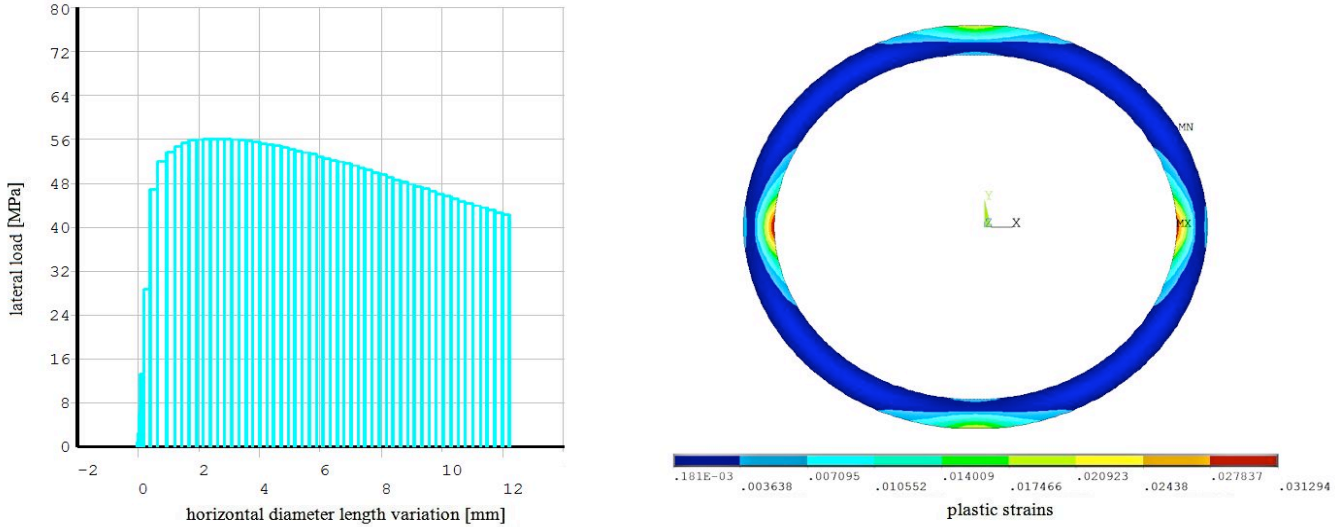

Figure 7: Results from FE analysis ($\bar{w}_1 = \omega R\ ,\ \psi_1 = 0\ ,\ \bar{w}_2 = 0\ ,\ \psi_2 = 0$).

with respect to the *x* axis, are defined around the ring circumference, as shown in Figure **9**. The amplitudes of these regions for $\theta \in [0, \pi]$ are, respectively,

$$\begin{aligned} &① \quad \theta \in [-\theta_c, \theta_c] \\ &② \quad \theta \in [\theta_c, \pi - \theta_c] \cup [\pi + \theta_c, 2\pi - \theta_c] \\ &③ \quad \theta \in [\pi - \theta_c, \pi + \theta_c] \end{aligned} \tag{4}$$

The representation of the stress-strain curves for carbon steels is assumed in the form of the Ramberg-Osgood (RO) power law,

$$\varepsilon^{(j)} = \frac{\sigma^{(j)}}{E} + \left(\varepsilon_y^{(j)} - \frac{\sigma_y^{(j)}}{E}\right)\left(\frac{\sigma^{(j)}}{\sigma_y^{(j)}}\right)^{\beta} \tag{5}$$

where β is a dimensionless coefficient, which for most engineering cases can be assumed ≥ 5, $\sigma_y^{(j)}$ is the j-th material region yield stress and $\varepsilon_y^{(j)}$ is the corresponding strain. Without loss of generality, the Young's modulus, *E*, is assumed to be the same for each material region.

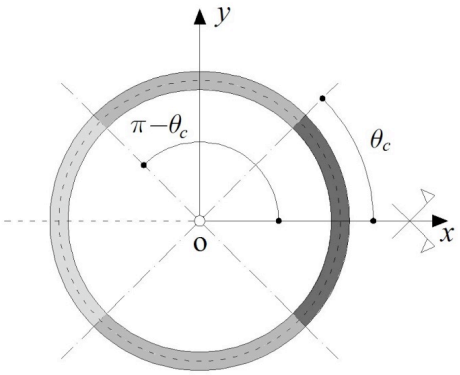

Figure 9: Non-homogeneous material regions.

With reference to Figure **9** the yield strengths for Regions ① and ③ have been obtained by amplifying the yield strength of Region ②, $E = 206.6GPa$, $\sigma_y = 561MPa$, $\varepsilon_y = 0.01$, $\beta = 7.625$ by a factor 1.1 and by reducing it by a factor 0.9. In this manner an increase in resistance is attributed to the Region ① and a corresponding decrease in resistance is attributed to Region ③.

The analytical treatment of the problem proposed in [11], leads to the determination of a collapse function, *f*. The function *f* can be plotted against the lateral load of the beam and the condition $f = 0$ is attained at impending collapse.

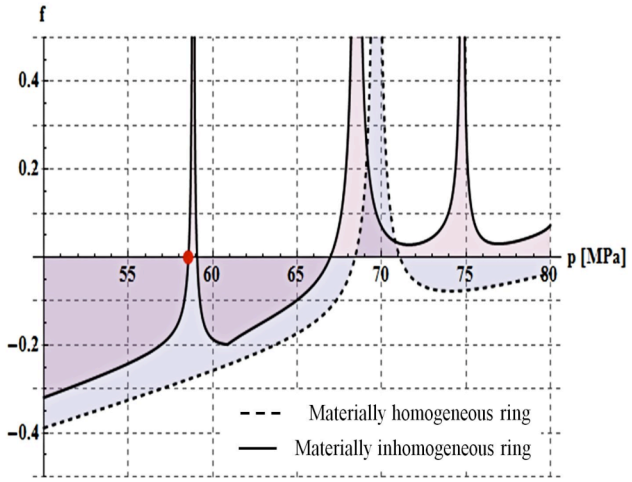

Figure 10: Plot of the collapse function, *f*, versus the lateral load, *p*, for a homogeneous (dashed line) and an inhomogeneous (continuous line) ring as in Table **3** for $\theta_c = \pi/4$, $\bar{w}_1 = 0$, $\bar{w}_2 = \omega R$.

Figure **10** shows the plot of the collapse function, *f*, versus the lateral load, *p*, for a homogeneous (dashed line) and an inhomogeneous (continuous line) circular beam for $\theta_c = \pi/4$ $n_1 = 2$, $n_2 = 3$ and $\bar{w}_1 = 0$, $\bar{w}_2 = \omega R$. The dimensions are the same of the rings of Table **1**.

From the plot it appears evident that for a pure three-wave initial imperfection the buckling load for the homogeneous beam results much lower than the one for the inhomogeneous beam. Moreover, both the buckling loads result in line with the experimental findings of Figure **4** (**a-c**) and (**d**), respectively.

This phenomenon can be attributed to an interference between the geometrical and material imperfections. In other words, the variability of material properties along the beam axis can induce a change of the collapsing modes, swinging the failure mode of the beam characterized by an initial imperfection of shape $\bar{w}_1 = 0$, $\bar{w}_2 = \omega R$ to the failure mode of a ring characterized by an initial imperfection of shape $\bar{w}_1 = \omega R$, $\bar{w}_2 = 0$.

Most importantly, it is worth underlining that Figure **11** shows the presence of a peak at the red dot which can be considered a sort of concealed well in the load-yielding plot. This sort of peaks, which can assume a very narrow shape depending on the geometrical and material properties of the beam, can turn sometimes difficult to trace numerically and, in case of an appreciable material inhomogeneity along the ring circumference, should be taken into account in order to interpret the experimental tests.

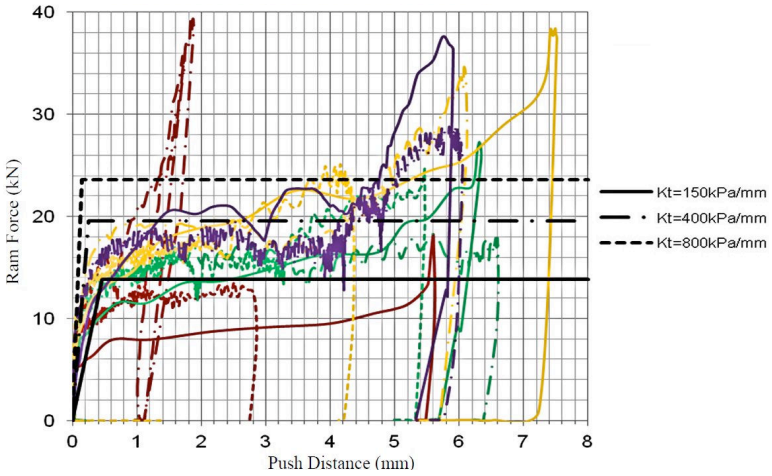

Figure 11: Push-out test results for different external pressure values [7].

5. FRICTION BETWEEN O-RINGS AND THE PLATES OF THE TEST RIG

In order to quantify the radial restraint induced by the O-rings, reference is made to push-out tests performed for the South Stream Ring Collapse Test Program [7]. The South Stream Offshore Pipeline project was aimed to the installation of a pipeline from the Russian shore of the Black Sea, through Turkish waters, to the Bulgarian shore, in water depths ranging up to 2200 m. A large number of ring specimens, manufactured from base plate material produced by several plate mills, were supplied from Europe and Asia. All the specimens were characterised by an external diameter (OD) equal to 812.8 mm (32 in) and a nominal wall thickness equal to 39 mm. Execution of the ring tests was performed by C-FER at their test facilities in Edmonton, Canada, under careful procedure and quality control.

The global O-ring friction properties were obtained by means of measurements of hydraulic ram force versus push distance, as shown in Figure **11**. The tests were performed for several values of hydrostatic pressure.

The scatter and the noticeable irregularity in the results is evident from the plots of Figure **11**, which also shows three possible modelling laws of the phenomenon, assumed by Selker *et al*. [7], of the type

$$\tau(\theta) = K_t w(\theta) \quad \text{if } K_t w(\theta) < 2\mu_s \sigma_n \qquad (6)$$

$$\tau(\theta) = 2\mu_s \sigma_n \quad \text{otherwise}$$

μ_s being the static coefficient of friction and σ_n the normal pressure exerted on the top and bottom surfaces of the tested ring. Under the assumption that, on account of the deformation of the O-rings, the contact between the test ring and the plates of the rig behaves as a linear spring until the plateau value $2\mu_s\sigma_n$ is reached (see Figure **11**), K_t represents the stiffness of this ideal spring. The coefficient 2 in the second of Eqs.(6) takes into account the fact that two O-rings, top and bottom, seal the test ring inside the rig.

Given the difficulty of interpretation of the data in Figure **11**, mostly with respect to the push distance at which the first slipping occurs, it is here believed that the most convenient approach to represent the possible restraint due to the friction between the seals and the ring sample may consist in making reference to a modified Coulomb's law of friction. Consequently, contact friction directed in the direction opposite to the ring displacement inside the test rig can be described, for each of the O-rings, by a relationship of the type

$$\begin{aligned} &\tau \le \mu_s \sigma_n \quad \text{when no slip occurs} \\ &\tau = \mu_k \sigma_n \quad \text{when slip occurs} \end{aligned} \qquad (7)$$

μ_s and μ_k being the static and kinetic coefficient of friction, respectively, and σ_n the normal pressure exerted on the top and bottom surfaces of the tested ring. An exponential decay relationship can be assumed to link the static and kinetic coefficient of friction as function of the slip velocity, $\dot{\gamma}_{eq}$,

$$\mu = \mu_s + \left(\mu_s - \mu_k\right) e^{-\psi \dot{\gamma}_{eq}} \qquad (8)$$

where ψ is a scalar.

The test setup has been reproduced in its governing aspects by means of a commercial Finite Element

package [18], and parametric analyses have been performed in order to investigate the influence of friction on the collapse.

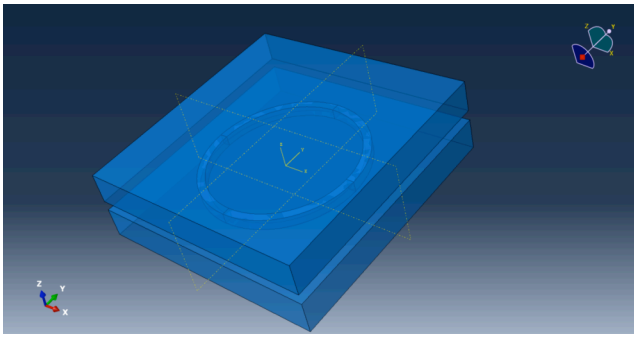

Figure 12: FE model of the testing device.

The testing device has been modelled using two stiff plates, as shown in Figure **12**. The upper plate is allowed to move in the *z*-direction, so that when a sealing vertical load is applied, a vertical pressure is transmitted to the tested ring. The plates measure 1200 x 1200 *mm*.

Top and bottom plates are linearly elastic. The material model shown in Figure **13** [7] has been implemented for the ring under test.

The adopted contact model (so-called "hard-contact") conforms to Eqs.(7) and also implies that:

- the surfaces transmit no contact pressure unless the nodes of the two surfaces are in contact;
- no penetration is allowed at each constraint location;
- there is no limit to the magnitude of contact pressure that can be transmitted when the surfaces are in contact.

In order to setup a sensitivity assessment, two pairs of friction coefficients (static/kinetic) have been adopted, i.e. 0.2/0.16 and 0.4/0.32.

The loading is applied in subsequent steps: first, a vertical pressure of 50 kPa is applied on the top surface of the upper plate; second, a hydrostatic pressure is progressively applied to the lateral surface of the test ring. The maximum value of the hydrostatic pressure, $p_{\max}$, is 60 MPa.

In such a manner the lowest kinetic coefficient of 0.16 gives origin to a value of the ram force equal to 24 kN, which corresponds to the highest value represented in Figure **11**.

The results of the analyses are shown in Figure **14**.

It is immediate to notice that in the frictionless case the collapse pressure results equal to 33.6 MPa, which is the result provided by the analytical formulation proposed in [9] for a two-wave imperfection shape and $\omega = 1/1000$. In the case of friction coefficients equal to 0.2/0.16, the collapse pressure results equal to 34.8 MPa, which approximately corresponds to the lowest value found in the South Stream Ring Collapse Test Program. In the case of friction coefficients equal to 0.4/0.32, the collapse pressure results equal to 40.8 MPa, which approximately corresponds to the highest value found in the South Stream Ring Collapse Test Program. Incidentally, this is also about the result provided by the analytical formulation proposed in [9] for a three-wave imperfection shape and $\omega = 1/1000$.

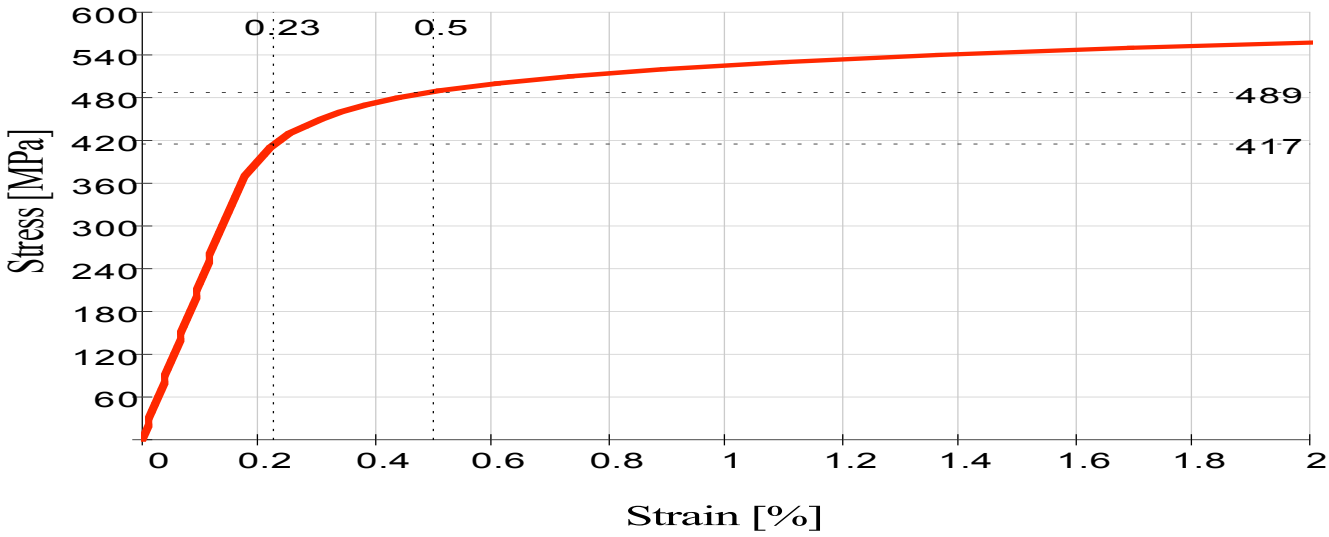

Figure 13: Ramberg-Osgood fit of the coupon test results (E=221 GPa, ν =0.3).

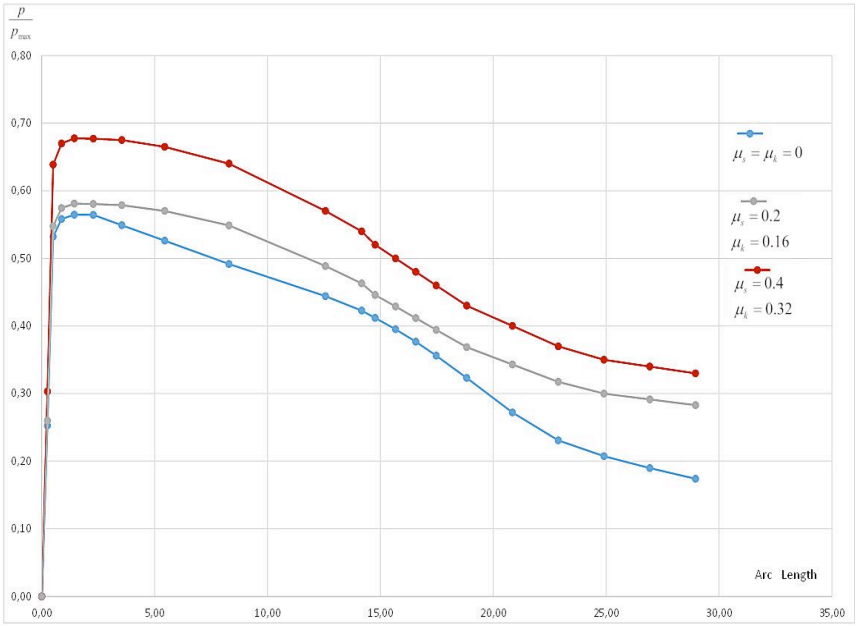

Figure 14: Results from FE analyses: influence of friction.

6. CONCLUSIONS

The ring test procedure recently used in manufacturing procedure qualification tests (MPQT) of offshore pipelines projects has been analysed, together with experimental results. The attention has been focused on three different parameters, i.e.: initial out-of-roundness of the ring, variation of the material properties of the pipe, friction between O-rings and the plates of the test rig.

The heterogeneity in some experimental results is likely to be due to the combination of the analysed factors and it is concluded that further experimental investigation is needed for a conclusive assessment of the procedure.

ACKNOWLEDGEMENTS

The present study has been motivated and supported by Verderg Ltd. The authors are grateful to Alastair Walker, Peter Roberts and Ian Nash for the useful discussions and encouragement.

REFERENCES

[1] Roberts PM, Walker AC. Method and apparatus for pipe testing. United States Patent no. 20100212405, 2010.

[2] Guarracino F, Fraldi M, Giordano A. Analysis of testing methods of pipelines for limit state design, Applied Ocean Research 2008; 30: 297-304. http://dx.doi.org/10.1016/j.apor.2008.12.003

[3] Guarracino F, Walker AC, Giordano A. Effects of Boundary Conditions on Testing of Pipes and Finite Element Modelling. Int J Press Ves Piping 2009; 86: 196-206. http://dx.doi.org/10.1016/j.ijpvp.2008.09.009

[4] Guarracino F. A Simple Formula for Complementing FE Analyses in the Estimation of the Effects of Local Conditions in Circular Cylindrical Shells CMES 2011; 72 (3): 167-184. http://dx.doi.org/10.3970/cmes.2011.072.167

[5] Tata Steel. Ring Collapse Testing Data. Internal Report. Tata Steel Tubes: Rotherham, UK 2011.

[6] Nash I, Carr P. The production and testing of meidp line-pipe for 3500m application. Proceedings of the International Offshore and Polar Engineering Conference 2013; 14-23.

[7] Selker R, Ramos PMC, Liu P. Interpretation of the South Stream Ring Collapse Test Program Results, Proceedings of the 24th International Ocean and Polar Engineering Conference, Busan. South Korea 2014; 2: 88-95.

[8] Det Norske Veritas. Submarine Pipeline Systems. DNV-OS-F101. Høvik Bærum Norway 2007.

[9] Fraldi M, Guarracino F. An improved formulation for the assessment of the capacity load of circular rings and cylindrical shells under external pressure. Part 1. Analytical derivation. Thin-Walled Structures 2011; 49: 1054-1061. http://dx.doi.org/10.1016/j.tws.2011.03.014

[10] Fraldi M, Freeman R, Slater S, Walke AC, Guarracino F. An improved formulation for the assessment of the capacity load of circular rings and cylindrical shells under external pressure. Part 2. A comparative study with design codes prescriptions, experimental results and numerical simulations. Thin-Walled Structures, 2011; 49: 1062-1070. http://dx.doi.org/10.1016/j.tws.2011.03.013

[11] Fraldi M, Guarracino F. Towards an accurate assessment of UOE pipes under external pressure: Effects of geometric imperfection and material inhomogeneity. Thin-Walled Structures 2013; 63: 147-162. http://dx.doi.org/10.1016/j.tws.2012.10.007

[12] FARO Technologies. FaroArm® Manual. FARO Technologies. Inc Lake Mary FL 32746 USA, 2009.

[13] Fraldi M, Guarracino F. Stability analysis of circular beams with mixed-mode imperfections under uniform lateral pressure, Advances in Mechanical Engineering Volume 2014; Article number 294507. http://dx.doi.org/10.1155/2014/294507

[14] Guarracino F. Considerations on the numerical analysis of initial post-buckling behaviour in plates and beams. Thin-Walled Structures 2007; 45: 845-848. http://dx.doi.org/10.1016/j.tws.2007.08.004

[15] Guarracino F, Walker AC. Some Comments on the Numerical Analysis of Plates and Thin-Walled Structures. Thin-Walled Structures 2008; 46: 975-980. http://dx.doi.org/10.1016/j.tws.2008.01.034

[16] Forde WRB, Stiemer SF. Improved Arc Length Orthogonality Methods for Nonlinear Finite Element Analysis. Computers & Structures 1987; 27: 625-630. http://dx.doi.org/10.1016/0045-7949(87)90078-2

[17] Crisfield MA. Non-linear Finite Element Analysis of Solids and Structures. Vol. 2, Advanced Topics. John Wiley & Sons. Chirchester 1987.

[18] Simulia. ABAQUS 6.1.3 User's Manual. Dassault Systèmes Simulia Corp Providence Rhode Island 2014.

Received on 16-11-2014 Accepted on 25-11-2014 Published on 20-04-2015

DOI: http://dx.doi.org/10.15377/2409-787X.2015.02.01.2